Atomistic mechanism for vacancy-enhanced grain boundary migration

Dengke Chen, Shuozhi Xu, and Yashashree Kulkarni

Phys. Rev. Materials **4**, 033602 — Published 6 March 2020

DOI: 10.1103/PhysRevMaterials.4.033602

Atomistic mechanism for vacancy-enhanced grain boundary migration

Dengke Chen
Woodruff School of Mechanical Engineering, Georgia Institute of Technology, GA, USA

Shuozhi Xu
California NanoSystems Institute, University of California, Santa Barbara, CA, USA

Yashashree Kulkarni*
Department of Mechanical Engineering, University of Houston, TX, USA

(Dated: February 14, 2020)

Mechanical behavior of polycrystalline materials is intimately connected to migration of grain boundaries which in turn is dramatically impacted by the presence of defects. In this letter, we present atomistic simulations to elucidate the elementary mechanism that dictates the role of vacancies in enhancing grain boundary migration via shear coupled normal motion. The minimum energy pathway and the associated energy barriers are calculated using the nudged elastic band method. Fully three-dimensional atomistic simulations provide excellent verification of the three-dimensional disconnection model and furnish quantitative evidence that vacancies facilitate grain boundary migration by weakening the line tension of a disconnection loop. It is also revealed that vacancies serve as energetically favorable sites for the nucleation of grain boundary disconnections, thereby inducing shear-coupled grain boundary migration.

I. INTRODUCTION

Grain boundaries (GBs) are key players in the plasticity, damage, and failure of polycrystalline materials [1–3]. A quantitative description of GB-mediated processes, such as migration, sliding and defect interactions, is hence vital for optimizing the properties of the polycrystal through mechanical processing and has been the subject of long-standing interest [4–19].

At low temperatures, a dominant mechanism for GB migration for a certain class of GBs, specifically, the coincident site lattice (CSL) GBs is known to be the shear-coupled normal motion[20, 21]. Shear-coupled normal motion occurs by the displacement of the GB normal to its plane due to resolved shear stress parallel to the GB plane. The motion is quantified by a geometric factor known as the coupling factor, $\beta = v_{||}/v_n$, which refers to the ratio between the applied shear velocity ($v_{||}$) and the resulting normal GB velocity (v_n). Several studies over the past years have provided insights into the dependence of the shear-coupled migration on GB geometry, temperature, and applied shear stress [20–28].

Using the nudged elastic band (NEB) method[29, 30], Combe and co-workers [24] investigated the migration of a $\Sigma13(320)$ GB in a copper bicrystal. They provided detailed evidence that thermally activated two dimensional (2D) shear-coupled GB migration occurs through a pair of parallel disconnections, each consisting of a dislocation and a step [4, 31]. However, three dimensional (3D) disconnection theory [4], which in principle is closer to reality, is still confined to theoretical analysis, and has not been verified through atomistic simulations or experiments to the best of our knowledge.

In addition, studies have probed the influence of impurities on GB motion [32–35] since GBs are known to be effective sinks for defects, especially point defects. Conventional understanding is that point defects, including vacancies, interstitials and substitutional atoms, have a drag effect thereby hindering GB migration [32]. Quite interestingly, some recent studies have reported that vacancies might enhance GB sliding [33] or body-centered cubic twin migration [36]. Thus, there is a need to investigate the elementary mechanism that leads to this rather unusual phenomenon by which vacancies might promote GB motion.

In the present study, we employ NEB simulations to provide the first verification of the 3D disconnection theory for GB migration. Furthermore, our NEB calculations elucidate the role of vacancies in shear-coupled migration of a certain class of GBs. It is revealed that vacancies facilitate the nucleation of GB disconnections by weakening the line tension of the disconnection loop and lowering the energy barrier for shear-coupled migration. The detailed elementary mechanism for the process is furnished by quasi 2D NEB calculations. The rest of the paper is organized as follows. In Section II, we describe the 3D simulation setup, details of the NEB calculations and formation energies for various vacancy sites in the GB. In Section III, we provide the representative 3D NEB results for GB migra-

* ykulkarni@uh.edu

tion with/without vacancies and investigate the effect of vacancy distribution and numbers. Section IV reveals the mechanism of vacancy-enhanced migration through atomistic/mesoscopic views and verifies the phenomenon through molecular dynamics (MD) simulations at room temperature. The summary and potential ramifications of these findings are discussed in Section V.

II. SIMULATION METHODS

A. Simulation setup

For our 3D atomistic simulations, we consider a copper bicrystal with a Σ13(320) symmetric tilt GB subjected to shear deformation (Fig. 1a). Our choice of this particular GB is dictated by the fact that it is a CSL boundary exhibiting shear-coupled normal motion, and its migration has been studied in 2D simulations previously [24]. All simulations are performed using the simulation package LAMMPS [37]. The embedded atom method (EAM) interatomic potential by Mishin et al. [38] is employed. Periodic boundary conditions are imposed in the lateral (Y and Z) directions whereas fixed boundary condition is imposed in the X direction. Two 1.5 nm thick slabs are fixed at the top and the bottom of the simulation cell and serve to exert the applied shear stress τ. Only the dynamic atoms within the simulation cell participate in the molecular statics (MS) simulations. The size of the 3D simulation cell is 103 Å × 130 Å × 123 Å.

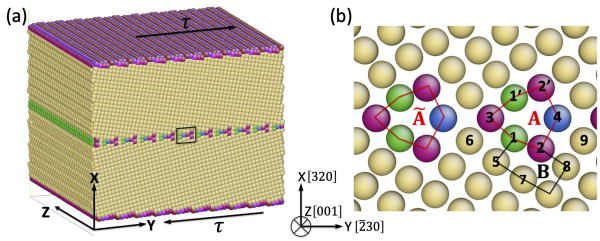

FIG. 1. (a) Atomistic structure of the simulation cell showing a GB in an FCC bicrystal. (b) Atomistic configuration of the Σ13(320) GB projected in the (X,Y) plane. Atoms are colored according to the coordination number CN (green: CN=10; red: CN=11; yellow: CN=12; blue: CN=13). Candidate vacancy sites around a repeating kite-shaped structural unit are labeled from 1 to 9. $1'$ and $2'$ are sites symmetric to 1 and 2 respectively.

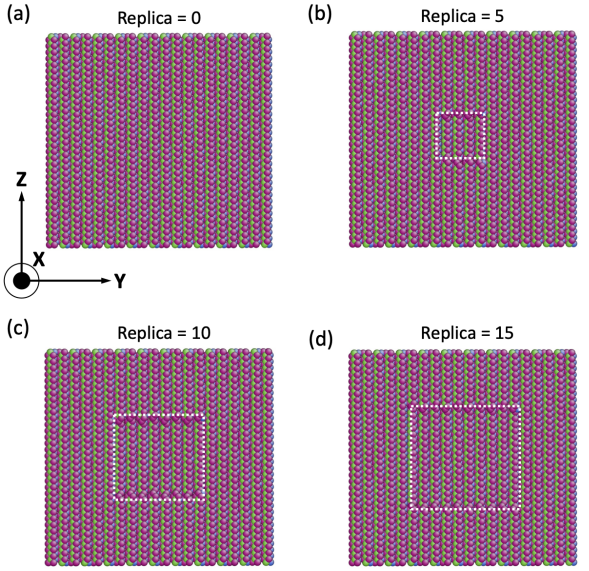

FIG. 2. Top view of several initial replicas for method 2 in our 3D NEB calculations. Disconnection nucleates in the form of similar rectangles (denoted by white-dotted line) with respect to the GB shape and expands gradually to the entire GB area. Atoms with coordination number CN = 12 are removed, thereby showing the GB in between the top and bottom surface.

B. NEB simulation details

$N(48)$ replicas were used to describe the minimum energy path (MEP). We imply initial configurations to mean the initial N replicas. After several time steps, they would converge to final configurations/replicas. For each time step, there are N replicas including first replica and end replica. The first and the end replica are fixed throughout the NEB calculation. The first replica is the original GB configuration without/with vacancies. The end replica is a configuration in which the entire GB has migrated by a step with the same shear strain as the first replica. We prepare two candidate initial configurations, or follow two initialization methods. Method 1 starts with a linear interpolation between the first replica and the end replica. In method 2, the initial intermediate replicas are generated with disconnection loops in the form of similar rectangles as shown in Fig. 2. To be specific, the disconnection loop of replica $i\,(1, 2, ..., N)$ has the size $(\frac{i}{N})^{2/3}L_Y \times (\frac{i}{N})^{2/3}L_Z$, where L_Y and L_Z are the dimensions of the GB in Y and Z directions respectively. For each value of shear stress, we choose the converged MEP with a lower energy barrier between these two methods. At low shear stress ($\tau < 450$ MPa), method 1 and 2 result in different MEPs. Specifically, method 2 yields a lower

energy barrier than method 1. At high shear stress ($\tau > 450\,\mathrm{MPa}$), which is the range we are interested in, both methods yield the same MEP which verifies the reliability of the NEB calculations.

C. Vacancy formation energy in a GB

The vacancy formation energy in a GB is defined as the energy required to move an atom from a certain GB site α to a perfect lattice site far away from the GB, i.e.

$$E_{\mathrm{f}}^{\alpha} = E_{\mathrm{GB}}^{\alpha} - E_{\mathrm{GB}} + E_{\mathrm{c}}, \tag{1}$$

where E_{GB}^{α} is the energy of defective GB with a mono-vacancy at site α, E_{GB} is the energy of the initial perfect GB, and E_{c} is the cohesive energy.

TABLE 1. Vacancy formation energies at different GB sites

Site	1	3	4	5	6	8	9
E_{f}(eV)	0.172	1.146	1.393	0.849	1.248	1.292	1.248

Table 1 summaries the vacancy formation energies at select sites (as shown in Fig. 1b) in the GB according to Eq. 1. It is seen that the vacancy formation energies vary widely from site to site. For most GB sites, the vacancy formation energies are much lower than that in the bulk (i.e. 1.272 eV [39]). However, there are still some GB sites, such as site 8, that have a higher vacancy formation energy than a perfect lattice site. It should be noted that for some sites, such as sites 2 and 7, the GB does not support vacancies at all. In other words, when an atom is removed from either site (2 or 7) to form a vacancy, the atom located in the nearest site 1 would fill the vacancy during the energy minimization process. Thus, the vacancy moves to site 1. The most important observation is that there exists a pair of energy-favorable vacancy formation sites 1 and 1′ with formation energy (i.e. 0.172 eV) which is much lower than any other GB sites. This indicates that for dilute vacancy concentration, most vacancies should be located at sites 1 and 1′ after enough diffusion time.

Following the previous study [40], the concentration c_{α} of vacancies at a site α in a GB is defined by

$$c_{\alpha} = \exp\left(-\frac{E_{\mathrm{f}}^{\alpha} - T S_{\mathrm{f}}^{\alpha}}{k_{\mathrm{B}} T}\right). \tag{2}$$

Here, E_{f}^{α} is the vacancy formation energy at site α, S_{f}^{α} is the formation entropy, k_{B} is the Boltzmann constant and T is the temperature. In this study, the interaction between vacancies is neglected. Experimentally [41], the factor $\exp(\frac{S_{\mathrm{f}}^{\alpha}}{k_{\mathrm{B}}})$ ranges between 2 and 10, which is consistent with previous studies [40]. Here, we adopt the upper bound to make the effect of vacancies more prominent. For the 3D simulation cell, as shown in Fig. 1, there are a total of 680 candidate sites that are energetically favorable (i.e., site 1). So according to Table 1 and Eq. 2, it is estimated that there are at most 9 energy-favorable vacancies in the GB in thermodynamic equilibrium at room temperature (i.e., 300 K). Accordingly, we start with 9 vacancies each located at a neighboring site 1, as shown in Fig. 3. It is worth noting that the vacancies are discrete, individual point defects that remain well-separated and embedded in the GB after equilibration.

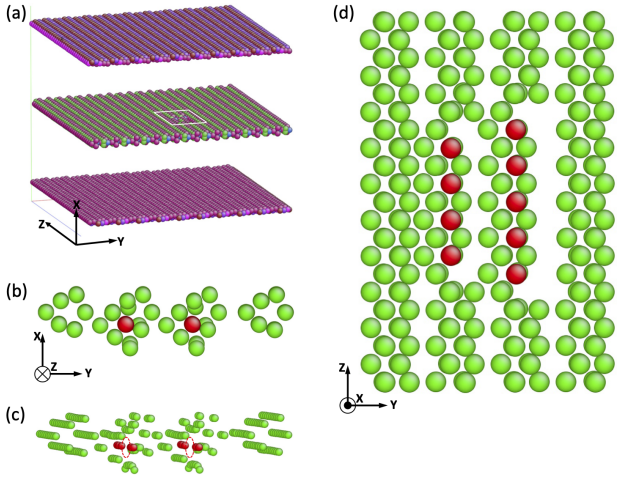

FIG. 3. Simulation setup and corresponding atomic configuration with 9 vacancies located in the GB. (a) Simulation cell which is identical to that shown in Fig. 1(a) except with 9 vacancies in the GB. Atoms with coordination number CN = 12 are removed, thereby showing the GB in between the top and bottom surface. (b)-(d) Different views of the atomistic structure of a portion of GB depicted by white square in (a). Atoms in the same column as the vacancies are labeled by red color; atoms in the neighboring columns are labeled by green color. (b) shows the projection of the GB atoms in the $X-Y$ plane. Vacancy sites are denoted by red circles in (c), in which there are 4 vacancies in the left column and 5 in the right, making a total of 9 vacancies. (d) shows the discrete vacancy positions in the Y-Z plane.

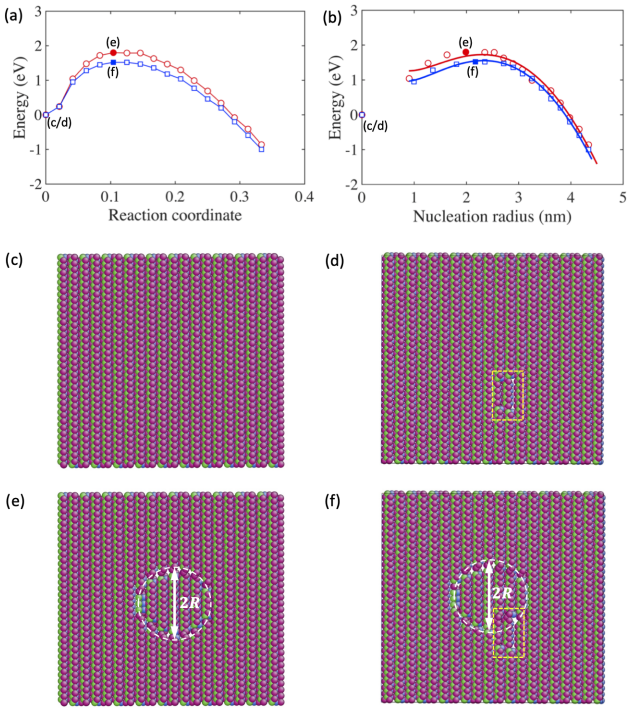

FIG. 4. 3D NEB results for GB migration without/with 9 vacancies under an applied shear stress $\tau = 529\,\mathrm{MPa}$. (a) MEPs of GB migration without vacancy (red circles) and with 9 vacancies (blue squares). (b) Associated MEPs as a function of the nucleation radius. (c)-(d) Top views of atomistic configurations for first replicas along the MEP for GB without/with vacancies. (e)-(f) Top views of atomistic configurations for saddle-point states along the MEP for GB without/with vacancies. Their corresponding energies are plotted as solid red circles and blue squares in (a) and (b). In (e) and (f), the disconnection diameter is denoted by 2R. White-dashed circles serve as guides to show circle-shaped nuclei. In (d) and (f), sites with vacancies are denoted by yellow-dashed rectangle.

III. RESULTS

A. Vacancy-enhanced migration

Fig. 4 shows the NEB results for GB migration in a 3D simulation cell without and with vacancies. Fig. 4(a) shows the converged MEP for shear-coupled migration of a perfect GB (red circles) and the same GB with vacancies (blue squares) at shear stress $\tau = 529\,\mathrm{MPa}$. In all the MEPs presented here, the reaction coordinate (RC) is defined as the normalized path length along the MEP, and the energy of first replica on the MEP is taken as zero. It is evident that the vacancies reduce the activation energy from 1.80 eV (red-solid circle) to 1.52 eV (blue-solid square). Fig. 4(b) shows the associated MEPs as a function of the nucleation radius. The atomistic configurations in Fig. 4(c) and (d) are the first states, corresponding to a local energy minimum on the MEPs. Fig. 4(e) presents the atomistic configuration at the saddle-point state (e) for migration of a perfect GB. It is seen that the shape of the disconnection loop is very close to a circular shape generated by the migration of discrete kite-shaped units. Consistent with prior theoretical prediction [4], the disconnection is nucleated in the form of a loop for 3D case. Fig. 4(f) shows the atomistic configuration at the saddle-point state (f) for a GB with vacancies. Since the disconnection loop would intercept with as many vacancies as possible (to maximally reduce the line tension and energy barrier, as will be explained later), the disconnection loop would deviate a little but still remain close to a circular shape. The results reveal that the disconnection loop nucleates around the vacancies (denoted by white circle) and then propagates, eventually resulting in GB migration (see [42]).

The nucleation and growth of the disconnection loop can be quantitatively described by the 3D disconnection model [4, 43]. According to the model, the total energy to form a disconnection loop with radius R is given by

$$E(R) = 2\pi R\bar{\Gamma}_{\mathrm{s}}h + E_{\mathrm{loop}} - p\pi R^2. \tag{3}$$

The first term is the excess energy arising from the disconnection step where $\bar{\Gamma}_{\mathrm{s}}$ is the effective line tension, and h is the step height which is 0.255 nm [24] for the $\Sigma13$ GB. The second term denotes the elastic energy of the disconnection loop which can be exactly expressed as [44]

$$E_{\mathrm{loop}} = 2\pi R\frac{2-\nu}{2(1-\nu)}\frac{\mu b^2}{4\pi}[-\ln(\tan\frac{\rho}{4R}) - 2\cos\frac{\rho}{2R}]. \tag{4}$$

Here, the Voigt average Poisson's ratio, $\nu = 0.324$, and the Voigt average shear modulus, $\mu = 55.2\,\mathrm{GPa}$, are elastic properties of the material. The values are taken for Cu based on the EAM potential used [38]. The Burgers vector b equals 0.1 nm [24] and ρ is the core radius of the disconnection loop. The last term in Eq. 3 is the work done by the driving stress p, which equals $\tau\beta$ where τ is the applied shear stress. Fig. 4(b) plots the associated disconnection loop energy $E(R)$ as a function of the disconnection loop radius R without/with vacancies. The discrete points are simulation results whereas the solid lines are based on Eq. 3 and Eq. 4 with $\bar{\Gamma}_{\mathrm{s}}$ and ρ used as fitting parameters. It bears emphasis that the excellent agreement between our atomistic simulations and the theoretical results provides the first direct verification of the 3D disconnection model for

GB migration. Furthermore, it is interesting to note that the model maintains its validity even in the presence of vacancies suggesting that the disconnection mechanism for GB migration remains the same. The disconnection core radius ρ is estimated to be 1.5 ± 0.1 nm in both cases (i.e., without/with vacancies) which is consistent with a prior work [45]. This implies that the 3D disconnection model, being a continuum model, is likely to break down when the nucleation radius is smaller than the disconnection core radius, which is about 1.5 nm for our case. Indeed, as seen in Fig. 4(b), the curve for the disconnection model starts deviating from the simulation results around 1 nm. $\bar{\Gamma}_s$ decreases from 345 mJ/m^2 for a perfect GB to 314 mJ/m^2 in the presence of vacancies. This suggests that the vacancies weaken the disconnection line tension thereby reducing the energy barrier for GB migration. It is also consistent with the observation that the disconnection loop nucleates around vacancies (see Fig. 4(f)). Fig. 5 reports the stress-dependent energy barrier for GB migration without/with vacancies using NEB calculations. The reduction in the energy barrier due to vacancies is in the range of $0.13 - 0.30$ eV.

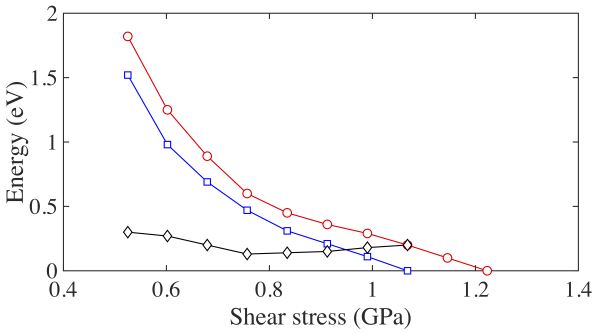

FIG. 5. 3D NEB calculations for the energy barrier of GB migration without (red circles) and with vacancies (blue squares) as a function of stress and the energy reduction due to vacancies (black diamonds).

B. Effects of vacancy distribution and number

In order to verify the vacancy-enhanced migration, we have studied three different cases of vacancy distributions (different arrangements of 9 vacancies). Figure 6 shows the stress-dependent activation energies for the GB without vacancies and with various vacancy configurations. The reduction in the energy barrier due to vacancies is evident for all three vacancy distributions. Here, vacancy distribution 1 refers to the atomistic configuration shown in Figure 3. The atomistic configurations of vacancy distribution 2 and 3 are shown in Fig. 7 and Fig. 8

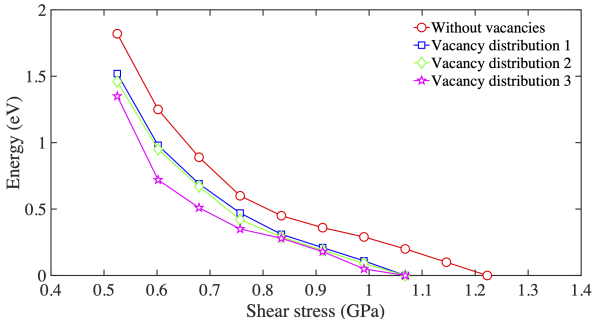

FIG. 6. 3D NEB calculations for the energy barrier of GB migration without vacancies (red circles), with vacancy distribution 1 (blue squares), distribution 2 (green diamonds) and distribution 3 (pink pentagram) as a function of stress.

respectively. Specifically, distribution 2 consists of 9 vacancies arranged in a single row and occupying site 1, whereas distribution 3 consists of 9 vacancies arranged randomly. It is worth noting that the vacancies are discrete and do not collapse into a void even for distribution 2.

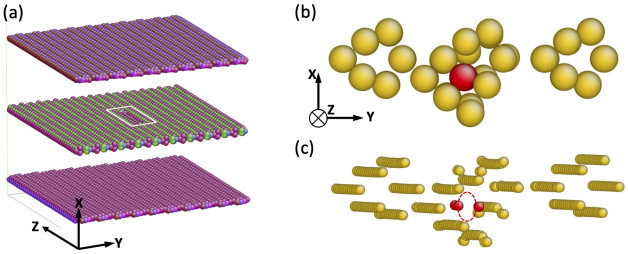

FIG. 7. Simulation setup and corresponding atomic configuration of 9 vacancies with distribution 2. (a) Simulation cell which is identical to those shown in Fig. 1(a) except with 9 vacancies in GB. Atoms with coordination number CN = 12 are removed, thereby showing the GB in between the top and bottom surface. (b)-(c) Inset images of atomistic structure of a portion of GB depicted by white square in (a). Here, atoms in the same column to vacancies are labeled by red color; other-column atoms are labeled by yellow color. Vacancy sites are denoted by red circles in (c), in which all the vacancies are in the same column.

In order to study the effect of number of vacancies, we use the random distribution of vacancies and vary the number from 1 to 11. Fig. 9 shows the activation energies without vacancy and with different number of vacancies arranged randomly. Here, number i means that there are i vacancies located at sites 1 from positions 1 to i as shown in Fig. 8(c). It is evident that energy barrier decreases with increasing vacancies. The reduction of the energy barrier depends on how many vacancies participate in the nu-

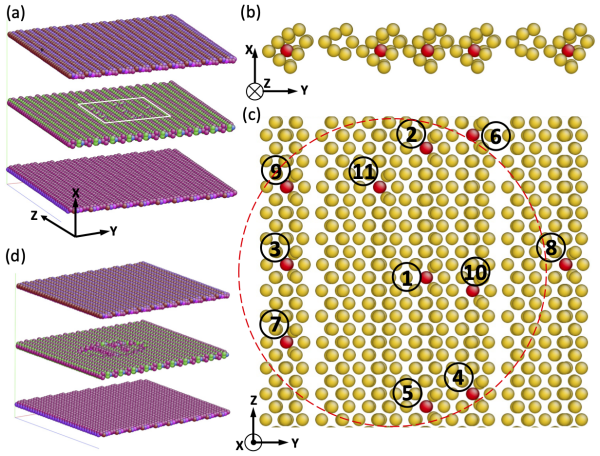

FIG. 8. Simulation setup and corresponding atomic configuration of randomly arranged vacancies with distribution 3. (a) Simulation cell which is identical to that shown in Fig. 1(a) except with 9 vacancies (numbered 1 to 9 in (c)) in the GB. Atoms with coordination number CN = 12 are removed, thereby showing the GB in between the top and bottom surface. (b)-(c) Atomistic structure of a portion of GB (depicted by white square in (a)) showing the arrangement of 11 vacancies. Here, atoms in the same direction as the vacancies projected in the X-Y plan are labeled by red color; other atoms are labeled by yellow color. Vacancy positions in the Y-Z plane are labeled by numbers from 1 to 11. (d) Atomistic configuration of saddle-point state along the MEP of the GB with first 9 vacancies (numbered 1 to 9 in (c)) under an applied shear stress $\tau = 529$ MPa. The red dashed circle in (c) schematically shows the disconnection loop connecting as many vacancies as possible at the configuration shown in (d).

cleation process in the saddle-point state, or in other words, how many vacancies are located near the disconnection loop and interact with it. Here, the activation volume is the disk-shaped volume with radius R and height h, or the projected area of the GB with radius R. Quantitatively, it is defined as the derivative of the energy with respect to the applied stress [46] and usually decreases with increasing stress. In Fig.8(d), besides number 1 vacancy, the other 8 vacancies (2,3,...9) have the opportunity to be simultaneously located around the disconnection loop at the saddle-point state (as schematically shown by the red-dashed circle in Fig. 8(c)). It follows that they can reduce the line tension of the disconnection and the energy barrier of GB migration as much as possible so that the energy reduction is largest among all three cases in Fig. 6 under an applied shear stress of $\tau = 529$ MPa. With increasing stress, the activation volume eventually becomes so small that only few vacancies (one or two for any vacancy distributions) need to be located around the dislocation loop to reduce the energy barrier. This explains why, at high stress, the reduction in energy barrier for different vacancy distributions is very close to each other. However, a more quantitative study of the dependence of the activation barrier on the vacancy distribution entails further theoretical analysis and simulations which will be part of our future work.

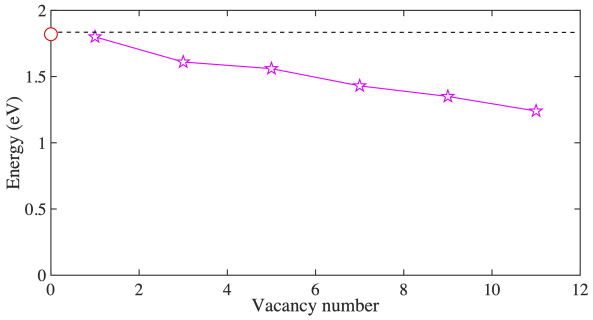

FIG. 9. 3D NEB calculations for the energy barrier of GB migration without vacancies and with varying number of vacancies under an applied shear stress $\tau = 529$ MPa. The black-dashed line is provided as a guide to the eyes and corresponds to the energy barrier without vacancies.

IV. DISCUSSIONS

A. Atomistic mechanism for vacancy-enhanced migration

In order to elucidate the elementary mechanism of vacancy-induced migration, we take recourse to quasi 2D simulations, where the out-of-plane thickness of the simulation cell is very small and has periodic boundary conditions (see Fig. 10) We recall that site 1 is the most energetically favorable for vacancy formation. Using energy minimization, Fig. 11 shows the relaxed configuration of the GB atoms after one atom is removed from site 1. Several nearest neighbor atoms surrounding the vacancy, including atoms at site 2 and site 1′, relax significantly towards the vacancy, which is consistent with previous studies [40, 47]. It is this displacement towards the vacancy site that triggers GB migration via transformation of the structural units from A to B under shear deformation.

Fig. 12 shows the NEB simulations of a 2D bicrystal with a mono-vacancy located at site 1. Converged MEPs for GB migration without/with vacancy in Fig. 12(a) are denoted by red and blue circles, respectively, at the same shear displacement ($s = 0.066$ nm). The MEP for the GB without va-

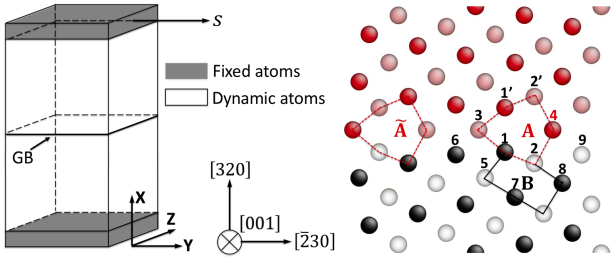

FIG. 10. (a) Schematic of the 2D simulation cell. The size of the 2D simulation cell is 103 Å × 13 Å × 14 Å. (b) Atomistic configuration of the Σ13(320) GB projected in the (X,Y) plane: Black (gray) and red (pink) atoms belong to different grains. Black (red) and gray (pink) atoms are in two alternate (100) planes. Candidate vacancy sites are denoted by the numbers from 1-9.

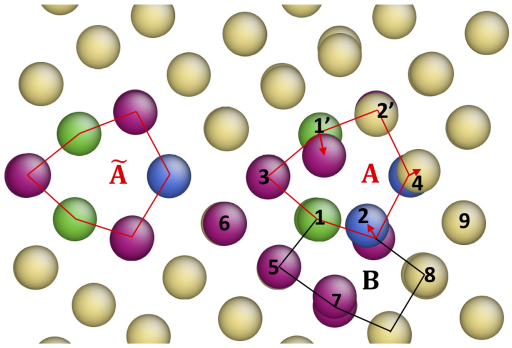

FIG. 11. Relaxed structure of the Σ13(320) GB with a mono-vacancy at site 1. Atoms are colored according to the coordination number. The red-dotted circle marks the vacant site. Since there are a total of four atoms for each site in the Z direction, the introduction of one vacancy still leaves three atoms, leading to visible atoms projected in the (X,Y) plane (green atoms marked as site 1). Relaxation of atoms surrounding the vacant site is denoted by red arrows.

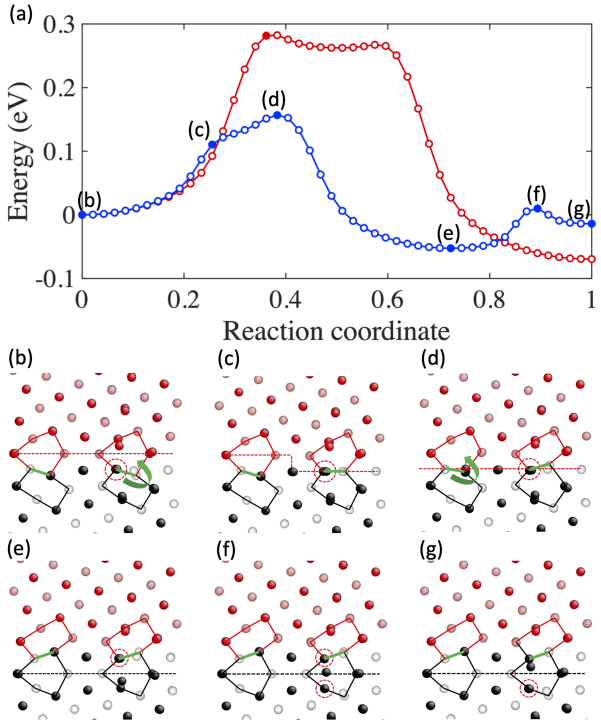

FIG. 12. 2D NEB results for the GB migration without/with mono-vacancy at a shear displacement s = 0.066 nm. (a) MEPs of GB migration without vacancy (red hollow circles) and with a vacancy (blue hollow circles). (b)-(g) Projection in the (x,y) plane of atomic configurations of replicas along the MEP for the GB with a vacancy. Their corresponding energies are plotted as solid-blue circles in (a). Red and black dotted lines are guided to the eyes through labeling the transient GB positions. For atomic configurations along the MEP for a perfect GB without vacancy, we refer the reader to [24].

cancies matches that reported by [24] which verifies our NEB calculation results. In the presence of a mono-vacancy, the activation energy for GB migration decreases by almost 50% from 0.29 eV to 0.16 eV. For intermediate configurations along the MEP for the perfect GB, we refer the reader to [24]. Fig. 12(b)-(g) show intermediate GB structures along the MEP for migration of a GB with a mono-vacancy. The GB structure in Fig. 12(b) is the first replica, corresponding to a local energy minimum on the MEP. The kite-shaped unit A is represented by red lines while the black lines denote the regular structural unit B. The green lines denote the bond between two atoms that belong to the two structural units. The mono-vacancy is marked by a red-dashed circle at site 1 of unit A.

First, the relaxation of atoms (at site 2 and 1') around the vacancy, in addition to the applied shear stress, triggers an anti-clockwise rotation of the green bond depicted by the green arrow (Fig. 12(b)). This initiates a transformation of the lattice structural unit B into a kite-shaped GB unit A (Fig. 12(c)). A concomitant step in the GB (depicted by the red dotted line) is observed between the left and right kite-shaped structural units. At the saddle-point state (Fig. 12(d)), the green bond continues to rotate and completes the transformation between structural units A and B. This vacancy-enhanced A - B unit transformation on the right facilitates the unit transformation on the left, thus yielding a lower energy barrier of 0.16 eV. When the transformation of the left structural units A - B is completed (Fig. 12(e)), it results in a local minimum energy state along the MEP (Fig. 12(a)). After this GB migration, the mono-vacancy diffuses to site 1 of the new GB (Fig. 12(e-g)). The associated energy barrier for vacancy diffusion is the relative energy difference

between state (e) and (f) along the MEP, yielding 0.08 eV. It is worth noting that the energy barrier of vacancy diffusion in the lattice is around 0.7 eV [48]. As such, this mono-vacancy prefers to move with the GB and continues to facilitate subsequent GB migration.

B. Line tension and varying GBs

The "effective line tension" in this work is the average energy penalty associated with a disconnection step h. From an atomistic view, the vacancies serve as energetically favorable sites for disconnection nucleation in a grain boundary, thereby facilitating shear-coupled migration. From a mesoscopic/defect-level perspective, as shown in Fig. 13(b) and (c), it is the vacancy that reduces the interaction between a "perfect" kite-shaped unit and an adjacent "defective" kite-shaped unit, leading to a lower energy penalty for the same disconnection step h. As such, it is reasonable to attribute the reduction of energy barrier to the reduction of line tension in meso-scopic level, as shown in Eq. 3.

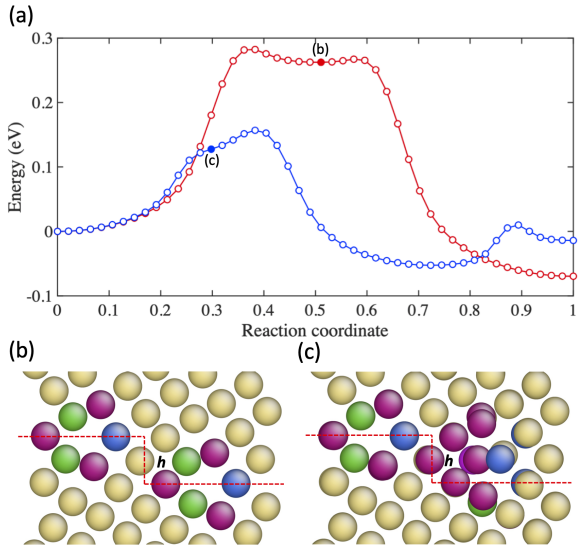

FIG. 13. 2D NEB results for the GB migration without/with mono-vacancy at a shear displacement $s = 0.066$ nm. (a) MEPs of GB migration without vacancy (red hollow circles) and with a vacancy (blue hollow circles). (b)-(c) Atomistic configurations associated with formation of step h without/with vacancy. Atoms are colored according to the coordination number. Red-dotted lines are guided to the eyes through labeling the step h.

To study the effect of vacancies on different GBs, we also examined several other CSL high-angle GBs (as shown in Fig. 14) using quasi 2D NEB calculations. It is seen from Fig. 15 that vacancies lower the activation barrier for migration in all cases. It also reveals that the reduction of line tension and energy barrier is associated with the spacing between adjacent kite-shaped structural units forming each GB.

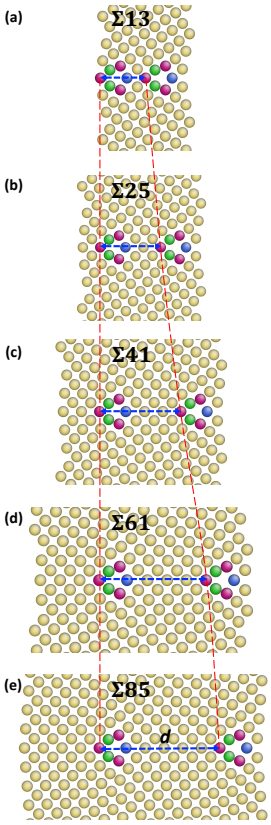

FIG. 14. Atomistic configurations of the simulation cells with (a) Σ13(320), (b) Σ25(430), (c) Σ41(540), (d) Σ61(650) and (e) Σ85(760) GBs. Atoms are colored according to the coordination number CN (green: CN=10; red: CN=11; yellow: CN=12; blue: CN=13). For each GB, the spacing between two adjacent kite-shaped structure unit is defined by d. The two dotted red lines serve as guides to show how the spacing d changes with the GB structure.

C. MD simulations at finite temperature

We performed several MD simulations to verify the vacancy-enhanced migration at finite temperature, both in 2D (Fig. 10) and 3D (Fig. 3) under constant shear stress. To implement constant stress conditions, we follow the method used for MD simulation of dislocation mobility in [49]. Multiple simulations (20 independent samples) were per-

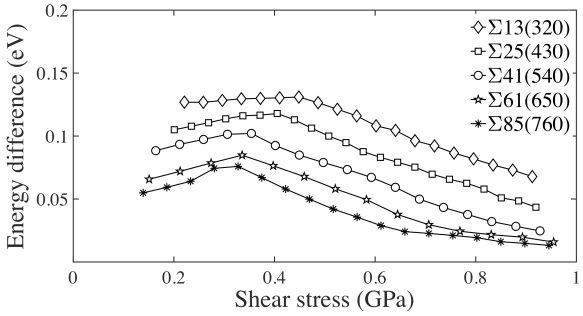

FIG. 15. Energy difference (i.e., the reduction of energy barrier) in the presence of the mono-vacancy versus applied shear stress for various GBs shown in Fig. 14.

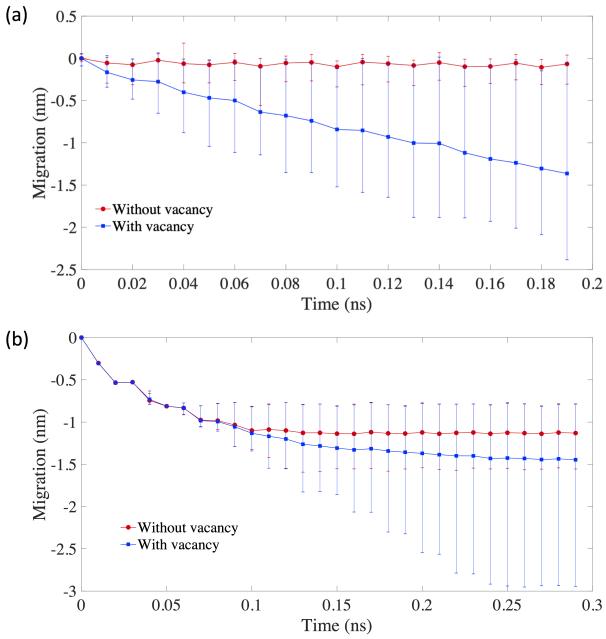

FIG. 16. MD simulations of shear-coupled GB migration at room temperature (a) under constant shear stress $\tau = 116\,\mathrm{MPa}$ for 2D simulation cell and (b) under constant shear stress $\tau = 316\,\mathrm{MPa}$ for 3D simulation cell. Error bar for each time intervals shows the fluctuation of GB displacement of 20 independent samples. Solid lines (blue or red) show the mean values.

formed in order to calculate the ensemble mean values. In order to accurately extract the average GB displacement for each time interval, we dynamically capture the GB profile based on the coordination number of each atom. Similar method has been utilized in other works [7, 8, 10]. Figure 16 shows the shear-coupled GB migration at room temperature in 2D/3D simulation cells without/with mono-vacancy. For 2D simulation cell, it is observed that GB migration in the presence of a mono-vacancy is almost one order faster than that GB without vacancy under the shear stress $\tau = 116\,\mathrm{MPa}$. Vacancy-enhanced migration is also observed for 3D simulation cell with 9 vacancies under the shear stress $\tau = 316\,\mathrm{MPa}$. Thus, these MD simulations clearly demonstrate the following: (1) the discrete vacancies do not diffuse away from the GB but instead stay in the GB as the boundary migrates. Thus, the effect of vacancies on the boundary migration continues; (2) The presence of vacancies facilitates shear-coupled GB migration.

V. CONCLUDING REMARKS

NEB calculations provide excellent verification of the 3D disconnection model and furnish quantitative evidence that vacancies facilitate shear-coupled migration of a certain class of GBs. Consistent with prior theoretical prediction [4], 3D atomistic modeling reveals that GB migration occurs via nucleation and growth of a disconnection in the form of a dislocation loop on the GB. Thus, from a continuum mechanics viewpoint, vacancies tend to weaken the line tension of a disconnection loop thereby promoting shear-coupled migration. 3D as well as quasi 2D simulations reveal that, from an atomistic viewpoint, vacancies serve as energetically favorable sites for disconnection nucleation of GB, thereby facilitating shear-coupled migration.

The study opens avenues for investigating the role of vacancies in migration and mobility of other GB structures. Moreover, the 3D NEB method employed here can be used to gain insights into the role of other types of defects on GB migration and consequently properties of polycrystalline materials. We believe that if the kite-shaped unit of the grain boundary retains its stable structure on adding dilute vacancies, we should see vacancy-enhanced migration. However, it is possible that there may be a change in deformation mechanism for GB migration when we look at GBs beyond this class. More systematic simulations would be needed for this study which is beyond the scope of this manuscript and will be pursued in our future work.

ACKNOWLEDGEMENT

YK gratefully acknowledges the support of NSF under grant DMR-1508484. DC and SX thank Mr. Wurong Jian and Mr. Yin Zhang for helpful discussions. We also acknowledge the use of the Maxwell cluster and the support from the Research Computing Data Core at the University of Houston. The work of SX was supported in part by the Elings Prize Fellowship in Science offered by the Califor-

nia NanoSystems Institute on the UC Santa Barbara campus.

[1] A. P. Sutton and R. W. Balluffi, *Interfaces in Crystalline Materials* (Oxford University Press, 2007).
[2] G. Gottstein and L. S. Shvindlerman, *Grain boundary migration in metals: thermodynamics, kinetics, applications* (CRC Press, 1999).
[3] H. Riedel, *Fracture at high temperatures* (Springer-Verlag, 1987).
[4] J. Han, S. Thomas, and D. Srolovitz, Progress in Materials Science **98**, 386 (2018).
[5] A. T. Lim, M. Haataja, W. Cai, and D. J. Srolovitz, Acta Mater. **60**, 1395 (2012).
[6] V. Agrawal and K. Dayal, J. Mech. Phys. Solids **85**, 291 (2015).
[7] D. Chen and Y. Kulkarni, MRS. Commun. **4**, 241 (2013).
[8] Z. T. Trautt, M. Upmanyu, and A. Karma, Science **314**, 632 (2006).
[9] S. M. Foiles and J. J. Hoyt, Acta Mater. **54**, 107 (2006).
[10] C. Deng and C. A. Schuh, Phy. Rev. Lett. **106**, 045503 (2011).
[11] D. Chen and Y. Kulkarni, Phys. Rev. Mater. **2**, 093605 (2018).
[12] S. Huang, D. Chen, D. L. McDowell, and T. Zhu, npj Comput. Mater. **3**, 28 (2017).
[13] Z. Wang, Q. Li, Y. Li, L. Huang, L. Lei, M. Dao, J. Li, S. Suresh, and Z. Shan, Nature Comm. **8**, 1108 (2017).
[14] Y. Wei, Y. Li, L. Zhu, Y. Liu, X. Lei, G. Wang, Y. Wu, Z. Mi, J. Liu, H. Wang, and H. Gao, Nature Comm. **5**, 3580 (2014).
[15] X. W. Gu, Z. Wu, Y. W. Zhang, D. J. Srolovitz, and J. R. Greer, Nano Lett. **13**, 5703 (2013).
[16] A. Dasgupta, P. Sharma, and K. Upadhyayula, Int. J. Damage Mech. **10**, 101 (2001).
[17] N. Admal, G. Po, and J. Marian, Int. J. Plasticity **106**, 1 (2018).
[18] I. Beyerlein, M. Demkowicz, A. Misra, and B. Uberuaga, Progress in Mater. Sci. **74**, 125 (2015).
[19] S. Thomas, K. Chen, J. Han, P. Purohit, and D. Srolovitz, Nature Comm. **8**, 1764 (2017).
[20] J. Cahn and J. Taylor, Acta Mater. **52**, 4887 (2004).
[21] J. Cahn, Y. Mishin, and A. Suzuki, Acta Mater. **54**, 4953 (2006).
[22] E. R. Homer, S. M. Foiles, E. A. Holm, and D. L. Olmsted, Acta Mater. **61**, 1048 (2013).
[23] F. Mompiou, D. Caillard, and M. Legros, Acta Mater. **57**, 2198 (2009).
[24] A. Rajabzadeh, F. Mompiou, M. Legros, and N. Combe, Phy. Rev. Lett. **110**, 265507 (2013).
[25] N. Combe, F. Mompiou, and M. Legros, Phy. Rev. B **93**, 024109 (2016).
[26] N. Combe, F. Mompiou, and M. Legros, Phy. Rev. Mater. **1**, 033605 (2017).
[27] N. Combe, F. Mompiou, and M. Legros, Phy. Rev. Mater. **3**, 060601 (2019).
[28] Q. Zhu, G. Cao, J. Wang, C. Deng, J. Li, Z. Zhang, and S. X. Mao, Nature Comm. **10**, 156 (2019).
[29] G. Henkelman, B. R. Uberuaga, and H. Jonsson, J. Chem. Phys. **113**, 9901 (2000).
[30] T. Zhu, J. Li, A. Samanta, H. G. Kim, and S. Suresh, Proc. Natl. Acad. Sci. **104**, 3031 (2007).
[31] J. P. Hirth and R. C. Pond, Acta Mater. **44**, 4749 (1996).
[32] M. I. Mendelev and D. J. Srolovitz, Model. Simul. Mater. Sci. Eng. **10**, R79 (2002).
[33] N. Du, Y. Qi, P. E. Krajewski, and A. F. Bower, Acta Mater. **58**, 4245 (2010).
[34] H. Sun and C. Deng, Comput. Mater. Sci. **93**, 137 (2014).
[35] D. Chen, T. Ghoneim, and Y. Kulkarni, Appl. Phys. Lett **111**, 161606 (2017).
[36] D. Song, X. Li, J. Xue, D. Hui, and Z. Jin, Phil. Mag. Lett. **94**, 361 (2014).
[37] S. J. Plimpton, J. Comp. Phys. **117**, 1 (1995).
[38] Y. Mishin, M. J. Mehl, D. A. Papaconstantopoulos, A. F. Voter, and J. D. Kress, Phys. Rev. B **63**, 224106 (2001).
[39] A. Suzuki and Y. Mishin, Interf. Sci. **11**, 425 (2003).
[40] M. R. Sorensen, Y. Mishin, and A. F. Voter, Phy. Rev. B **12**, 3658 (2000).
[41] W. Cai and W. Nix, *Imperfections in Crystalline Solids* (Cambridge University Press, 2016).
[42] See Supplemental Material at [] for videos of GB migration with and without vacancies.
[43] C. P. Race, J. von Pezold, and J. Neugebauer, Phys. Rev. B **89**, 214110 (2014).
[44] J. P. Hirth and J. Lothe, *Theory of dislocation* (Krieger Publishing Company, 1992).
[45] S. Xu, L. Xiong, Y. Chen, and D. McDowell, J. Mech. Phys. Solids **96**, 460 (2016).
[46] T. Zhu and J. Li, Progress in Materials Science **55**, 710 (2010).
[47] G. Lu and N. Kioussis, Phy. Rev. B **64**, 024101 (2001).
[48] T. Zhu, J. Li, and S. Yip, in *Nano and Cell Mechanics* (Wiley Online Library, 2013) pp. 313–338.
[49] D. L. Olmsted, L. G. H. Jr, W. A. Curtin, and R. J. Clifton, Model. Simul. Mater. Sci. Eng **13**, 371 (2012).